Earth and Planetary Science Letters 576 (2021) 117244

Contents lists available at ScienceDirect

Earth and Planetary Science Letters

www.elsevier.com/locate/epsl

Electrical resistivity imaging of continental United States from three-dimensional inversion of EarthScope USArray magnetotelluric data

Bo Yang [a,b], Gary D. Egbert [b], Huiqian Zhang [c,b], Naser Meqbel [d,e], Xiangyun Hu [a,*]

[a] Hubei Subsurface Multi-Scale Imaging Key Laboratory, Institute of Geophysics and Geomatics, China University of Geosciences, Wuhan, China
[b] College of Earth, Ocean, and Atmospheric Sciences, Oregon State University, Corvallis, OR, USA
[c] School of Earth and Space Sciences, Peking university, Beijing, China
[d] National Observatory, Rio de Janeiro, Brazil
[e] 3D Consulting-Geo GmbH, Berlin, Germany

ARTICLE INFO

Article history:
Received 25 April 2021
Received in revised form 5 October 2021
Accepted 8 October 2021
Available online xxxx
Editor: R. Bendick

Keywords:
USArray
magnetotellurics
continental US
upper mantle
water content

ABSTRACT

Long-period magnetotelluric (MT) sites, covering much of the continental United States (US) have been collected through the EarthScope USArray MT Transportable Array (TA) project. Previous regional studies using subsets of these data suggest large-scale variations in deep (sub-lithospheric) resistivity, often of significant amplitude. Here, we present a range of three-dimensional (3D) continental-scale electrical resistivity models from 3D inversion of the MT TA data, with a focus on testing robustness and resolution of this deep structure. The main features of our initial model, obtained with no constraints, are quite similar to those from previous studies, with significant (± 1 order of magnitude) lateral variations in deep resistivity. We show that data fit, as measured by global normalized root-mean-square misfit, is not increased by replacing structures below 200 km depth with layer averages. A more careful examination of residuals leads to further refinements, with a slight improvement in data fit. These include a moderately conductive mantle transition zone (13 Ω.m), and subtle ($\pm 1/4$ order of magnitude) lateral variations in resistivity below 200 km. In contrast to the initial results, these variations can be explained by reasonable variations in mantle temperature and hydration. Overall, our results suggest that the asthenospheric mantle at 200–275 km is nearly dry on average and at greater depths contains 150–300 ppm water. Lateral variations may be explained by this range of water content, or by temperature variations of 80–120°C. Patterns of resistivity variations below 200 km are consistent with known continental structure, and suggest deep roots (~250 km) beneath cratons, and perhaps also beneath the mid-continent rift. Reduced resistivity, likely requiring greater hydration (or higher temperatures), occurs beneath the North-central part of the continental US, the oldest part of the continent, and beneath the Yellowstone hotspot.

© 2021 Elsevier B.V. All rights reserved.

1. Introduction

The USArray magnetotelluric (MT) transportable array (TA) component of EarthScope is a powerful tool for studying the electrical structure and evolution of North America. Between 2006–2018, a total of 1116 long period (~10–20,000 s) MT sites were occupied (Schultz et al., 2006–2018), extending from coast-to-coast, and covering much of the continental United States (US) (Fig. 1), including the Northwestern US (2006–2011), the mid-continent (2011–2013), Eastern US (2014–2017) and Northern Great Plains (2017–2018).

A number of regional-scale inversions of these MT TA data, each covering a different area, reveal significant large-scale variations in deep resistivity (or its inverse conductivity) (e.g., Patro and Egbert, 2008; Meqbel et al., 2014; Bedrosian and Feucht, 2014; Yang et al., 2015; Murphy and Egbert, 2017). These have mostly been interpreted as variations in thickness of the lithosphere (e.g., between the Basin and Range, and adjacent cratons), or as suture zones penetrating deep into the lithosphere (e.g., Bedrosian and Feucht, 2014; Meqbel et al., 2014; Yang et al., 2015). There are also significant differences in deeper asthenospheric resistivity, both within individual models, and between different studies (e.g., Meqbel et al., 2014; Yang et al., 2015).

* Corresponding author.
E-mail address: xyhu@cug.edu.cn (X. Hu).

https://doi.org/10.1016/j.epsl.2021.117244
0012-821X/© 2021 Elsevier B.V. All rights reserved.

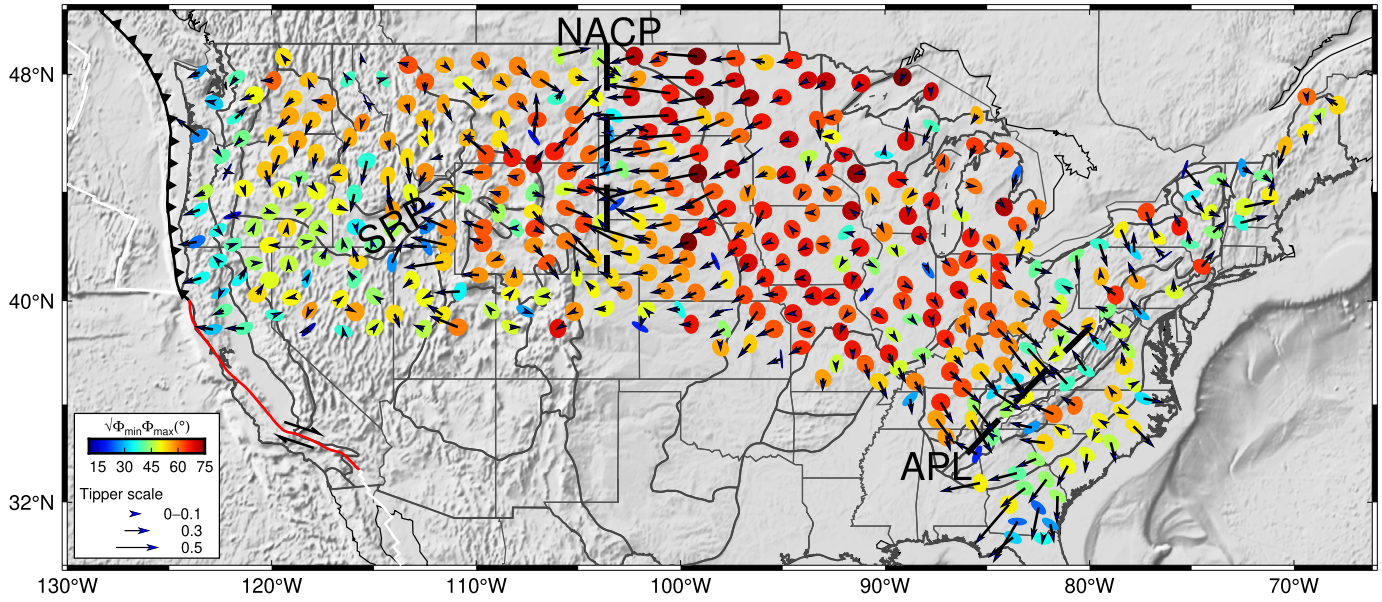

Fig. 1. Phase tensors and induction vectors for EarthScope MT sites used in this study, plotted on base map showing topography and major physiographic provinces. Abbreviations shown in black are as follows: APL, Folded Appalachians; NACP, North American Central Plains; SRP, Snake River Plain. Phase tensor ellipses shown (Caldwell et al., 2004) are for ∼12,000 s with color representing $\sqrt{\Phi_{min}\Phi_{max}}$. The predominance of high phase (> 45°) indicates generally increasing conductivity at great depth. The majority of phase values between NACP and APL are very high (> 60°), indicating a steeper conductivity gradient at depth in the center of the continent. As our inversion results show (Fig. 2(c-h)) this results primarily from a more resistive and thicker lithosphere in the center of the continent. Arrows represent real parts of induction vectors at ∼1,000 s with Parkinson sign convention (pointing towards higher conductivity). Vectors are large, and reverse direction crossing both the NACP and APL (dashed lines), indicating relatively narrow high conductivity anomalies. Additional localized conductivity anomalies, such as the SRP are also evident. All these conductive zones are also clear in our inversion results (Fig. 2c). (For interpretation of the colors in the figure(s), the reader is referred to the web version of this article.)

Due to the inherent non-uniqueness of MT data, it is essential to assess which features are robust before interpreting inversion results. Previous regional-scale studies using EarthScope MT TA data have mainly focused on lithospheric features. Beyond simple tests of depth resolution (e.g., Meqbel et al., 2014) robustness of deeper structure, in particular lateral variations in asthenospheric conductivity, has not been tested very carefully. In fact, because electrical resistivity is highly sensitive to water content and relatively insensitive to other factors (Karato, 2011), if the significant deep resistivity variations suggested by previous studies were robust, this would imply very significant variations in mantle hydration, with far-reaching implications for Earth's deep water cycle, mantle rheology, and geodynamics. Therefore, these variations in deep resistivity warrant thorough testing (e.g., Yang et al., 2015).

Here we explore the robustness of this deep structure by constructing three-dimensional (3D) inverse models for all of the continental US where MT TA data were readily available at the start of this study (Fig. 1). To do this, we invert all sites simultaneously, to guarantee consistency between different regions, and to allow more explicit tests of robustness of large-scale deep structures. As a first step we construct an unconstrained inverse solution, with a conventional application of the ModEM code (Kelbert et al., 2014). We then constrain deeper layers to be uniform (averages of the initial solution), and restart the inversion. Careful examination of the resulting long-period residuals reveals that further refinements to deep structure are necessary for an adequate data fit. To achieve this we use a combination of forward modeling and inversion, ultimately arriving at a final resistivity model which we interpret by comparison to laboratory electrical measurements and seismological observations. As we discuss this multi-step inversion process in some detail, a number of "intermediate" models (M2-M4) will be introduced in addition to the initial (M1) and final (M5) models. All models mentioned are summarized in Table 1. However, only the initial and final models are explicitly shown, or discussed in any detail. The remaining models represent steps toward the final solution, and are discussed only in terms of data misfit. As we show, through this process we arrive at a model with improved long-period data fit, that is also more physically consistent with other geophysical constraints.

2. MT data and 3D inversion

Theory and practice of MT are well reviewed in Simpson and Bahr (2005) and Chave and Jones (2012). In short, MT uses simultaneous measurements of the horizontal components of time varying natural electromagnetic (EM) fields on Earth's surface to reveal the electrical resistivity of the subsurface at depths ranging from tens of meters to several hundred kilometers. Penetration depths of the EM fields increase with increasing Earth resistivity, and with increasing period of the EM field variations. The USArray MT TA data were collected on a quasi-regular grid with approximately 70 km spacing, with typical site occupations of about 3 weeks. Such long-period (∼10–20,000 s) MT data are suitable for imaging resistivity structure from the middle crust to at least the top of the asthenospheric mantle (e.g., Meqbel et al., 2014). The MT transfer functions, estimated from time series using a standard robust remote reference method (Egbert and Booker, 1986), are freely available (Kelbert et al., 2011) and will be used for the 3D inversions discussed here.

Due to computational limitations we were forced to use a relatively coarse model grid, and to reduce to a carefully selected (and widely enough spaced, given the grid resolution) subset (423 of 1116) of MT TA sites, as shown in Fig. 1 and S1. Relatively shallow lateral variations in resistivity can result in quasi-static (independent of period) distortion of electric fields. This can be modeled in 3D using a grid of sufficient resolution, or by adding galvanic distortion parameters (Avdeeva et al., 2015); we use the first approach here. Miensopust (2017) concluded that horizontal cells about a fifth to a sixth of the spacing between neighboring sites would be sufficient to directly model galvanic effects. For MT modeling of the full TA dataset (as has been done in the regional inversions cited above), this implies a lateral cell size of about

12–15 km (e.g., Meqbel et al., 2014; Bedrosian and Feucht, 2014; Murphy and Egbert, 2017), although somewhat coarser resolution (20 km) has also been used (Yang et al., 2015). Using such fine resolution for the large area we consider would result in too many grid cells to be computationally practical. We thus select roughly half of the sites, maintaining quasi-uniform spacing, to allow use of a coarser grid (30 km spacing), and to make the inverse problem more computationally tractable.

Fortunately, the quality of the archived MT transfer functions have been rated using a scale from 1 to 5, with 5 indicating the highest quality (Imamura and Schultz, 2020). To select sites to be used for our study, we first set a minimum spacing of 120 km among sites with high quality ratings (4 or 5). Then, large gaps were filled in, using lower quality data (but still with at least a rating of 3), as necessary. Finally, to get more spatially uniform site coverage (at least in a subjective sense), we manually added and removed some sites. After constructing the 30 km numerical grid, we found that some sites near the coasts were not on land, and had to be excluded. The final result of this data selection process is shown in Fig. 1, with a total of 423 MT sites, approximately half of high quality (quality control rating of 4 or 5). A histogram of data errors for phases of off-diagonal impedance elements gives some indication of overall data quality (Fig. S2).

The 3D inversions were performed using ModEM (Egbert and Kelbert, 2012; Kelbert et al., 2014) to jointly invert all components of the impedance, together with vertical field transfer functions (VTFs). To avoid external source bias on the VTFs (e.g., Egbert, 1989), periods greater than 3,000 s were excluded. Thus, all of the 30 periods from 10 to 20,000 s were used for impedance, and 25 periods were used for VTFs, with bad data at a few periods for a few sites removed before inversion. Error floors were set the same for all impedance components as $\sqrt{|Zxy \times Zyx|} \times 0.05$. For the VTFs a constant value of 0.03 was used. If the calculated error floor was lower than the data error estimate, we used the actual data error. A nested inversion approach was used to reduce the size of the model domain, and thus grid size, while still allowing for possible influences from external electrical structures (e.g., the oceans) that are far from the area covered by MT sites (Meqbel et al., 2014; Murphy and Egbert, 2017). In this approach, there are two models with the same coordinate origin. A forward run with the coarser model is used to provide boundary conditions (BC) for a finer (nested) model that is almost fully covered by MT sites. In our application the coarser horizontal grid is of dimension 50×96 in x and y directions, with a resolution of 60 km in the center of the grid, padded by logarithmically spaced (factor of 1.3) layers extending to the side boundaries. The finer horizontal grid is 78×170 in x, y directions with a uniform resolution of 30 km. The resulting coarse grid covers an area of $5800 \times 8600\,\mathrm{km}^2$, in contrast to the $2300 \times 5100\,\mathrm{km}^2$ area of the nested grid used for the actual inversion. In the vertical direction, both models extends to a depth of 960 km, with logarithmically spaced layers starting from 50 m at the surface, increasing by a factor of 1.15, resulting in 57 layers. An additional 12 air layers were used to provide the upper BC.

We did approximately 10 inversion runs with varying inputs or control parameters (e.g., different prior model, model covariance) to arrive at the initial model presented in Fig. 2. The main inversion parameters for this model are as follows. The prior (and starting) model was a uniform 200 Ω.m half-space (based on the apparent resistivity averaged in the log domain over modes, sites, and periods), with a 0.3 Ω.m ocean, which was frozen in the inversion. The ModEM model covariance smoothing parameter was uniformly set to 0.2, with 2 smoothing passes in every direction. An overall normalized root-mean-square misfit (nRMS) of 1.96 was achieved after 180 iterations (Fig. 2a). If we ignore periods less than 50 s, the nRMS misfit is reduced to 1.68 (Fig. 2b), suggesting that the model is too coarse to fully model shallow structures (this is clearer in Fig. 4g). However, the overall fit is quite acceptable, and comparable to other published inversions using EarthScope TA data.

As the data cover a significant area, spherical effects should perhaps be considered (Grayver et al., 2019). Most significantly, impedances are expressed in a local geographic coordinate system, with the direction of the x-coordinate axis, when projected to the Cartesian system used by ModEM, varying across the array. We did tests accounting for this (i.e., rotating to a common coordinate system, defined at the center of the array), and obtained essentially identical results (Fig. S3). We therefore did not pursue this complication further.

3. Significant large-scale variations in deep resistivity

As depicted in Fig. 2, the main lithospheric features of our initial model are consistent with geological settings, and quite similar to those from previous studies (e.g., Meqbel et al., 2014; Bedrosian and Feucht, 2014; Yang et al., 2015; Murphy and Egbert, 2017), especially considering the lower resolution of both model and data constraints used in this study. For example, the conductive North Basin and Range and Snake River Plain in the west, the very conductive North American Central Plains anomaly (Kelbert et al., 2019), high conductivity beneath the Appalachians (Fig. 2c), and the thick resistive cratonic blocks in the North-Central US, and beneath the southeastern US (SEUS) (Fig. 2d) are all similar to major features in the cited studies. In general, lithospheric conductivity (Fig. 2c and Fig. 2d) is much higher, and depth to the lithosphere-asthenosphere boundary (LAB) shallower, in tectonically active regions (e.g., western US) compared to tectonically stable regions (e.g., central and eastern US, excluding the Appalachians) (Goes and van der Lee, 2002). In previous studies, high conductivities associated with arc magmatism, crustal extension, and mantle plumes, have been interpreted as partial melt and/or aqueous fluids (e.g., Meqbel et al., 2014). Along terrane boundaries, conductive features have been interpreted as sutures, most often explained as graphite and/or sulfide deposits penetrating deep into the lithosphere (e.g., Wannamaker, 2005). All of these features are seen in initial model (Fig. 2), albeit with lower resolution than in some previous studies.

There are also deeper (200–400 km) variations in resistivity in the initial model, as in earlier publications (e.g., Meqbel et al., 2014; Yang et al., 2015; Murphy and Egbert, 2017). Comparisons on selected transects (Fig. S1) reveal similarities, such as the very conductive feature beneath the Northern Rocky Mountains (Fig. 2(f-h)) which appears on the eastern edge of the model of Meqbel et al. (2014), but also differences. For example, in the study by Yang et al. (2015), smooth variations in deep (200–400 km, asthenospheric) resistivity (10–30 Ω.m), were found. In our model resistivities are more variable (1–100 Ω.m) and often much lower. And, in our model very high resistivities ($> 1000\,\Omega$.m) persist to great depth beneath the SEUS. As we discuss further below, these resistivities are unreasonably high, given expected temperatures at such depth, and they differ from preferred models presented in Murphy and Egbert (2017, 2019). In general, lateral variations seen in initial model at depths below 200 km have a larger range than those seen in most previously published results. Furthermore, as the previous regional-scale studies typically did not focus on these deep structures, they have so far not been extensively tested.

4. Resistivity below 200 km

To assess the robustness of features constrained by the inversion, we do a number of additional runs, both forward and inverse. To keep track of these, and to streamline discussion, we use the

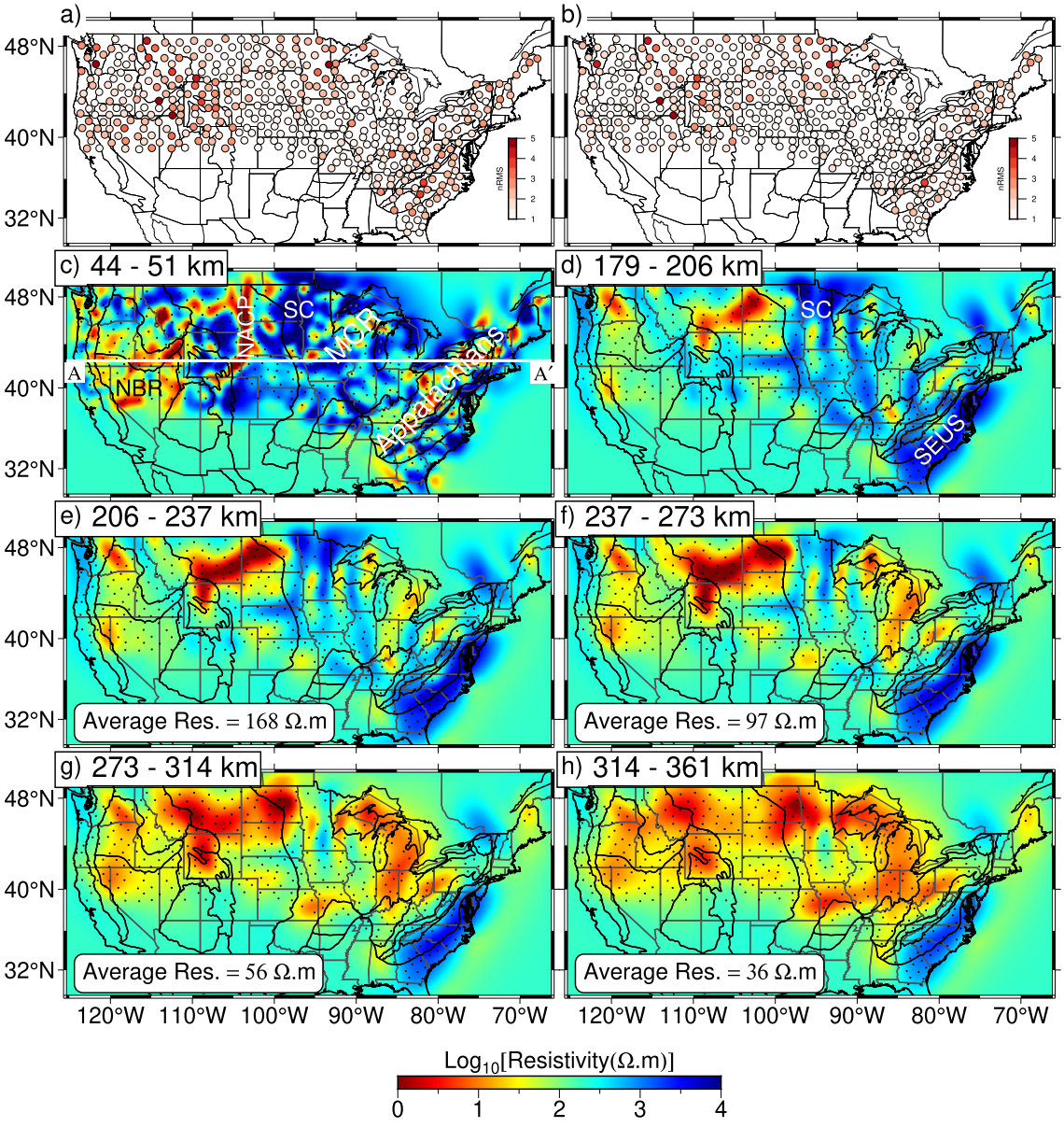

Fig. 2. Site by site nRMS for (a) all periods and (b) periods large than 50 s; (c-h) selected depth sections for initial resistivity model. The white solid line AA′ along latitude 42.5°N in (c) denotes the transect used in Fig. 3(a-c). Average log resistivity of each depth slice, computed as the mean over area with data coverage, is shown for layers below 200 km. NBR: North Basin and Range; MCR: Midcontinent Rift; SC: Superior Craton; SEUS: Southeastern US.

Table 1
Summary of models and associated normalized root-mean-square misfit (nRMS) discussed in this paper. The nRMS of each model indicates the nRMS for all periods, periods less than 3,000 s, and periods greater than 3,000 s, respectively, relative to the measured data. For M2 only forward modeling was done; all other models were obtained by inversion. BC: boundary conditions. Only M1 (initial inverse solution), and M5 (the final preferred solution) models are presented and discussed in detail, with only selected results and misfit statistics presented for the intermediate models M2-M4. Model M6 is very similar to M5, and is also not presented in any detail.

Model	nRMS	Description
M1	1.96, 2.00, 1.62	initial (unconstrained) inverse model
M2	2.07, 2.06, 2.23	layers below 200 km averaged from M1
M2.1	1.87, 1.88, 1.83	freeze M2 below 200 km, restart inversion; same BC as M1
M3.1	1.83, 1.85, 1.64	as M2.1 but use M1 layer averages to define BC for nesting model
M3.2	1.82, 1.85, 1.53	as M3.1 but set MTZ to 13 Ω.m and restart inversion
M4.1	1.95, 1.97, 1.78	as M3.1 but with depth cutoff of 150 km
M4.2	1.94, 1.97, 1.68	as M4.1 but set MTZ to 13 Ω.m and restart inversion
M5	1.81, 1.84, 1.49	restart inversion from M3.2 using smoothed off-diagonal ϕ, ρ_a residuals; freeze model except 200–400 km
M6	1.81, 1.84, 1.49	as M5 but also unfreeze MTZ

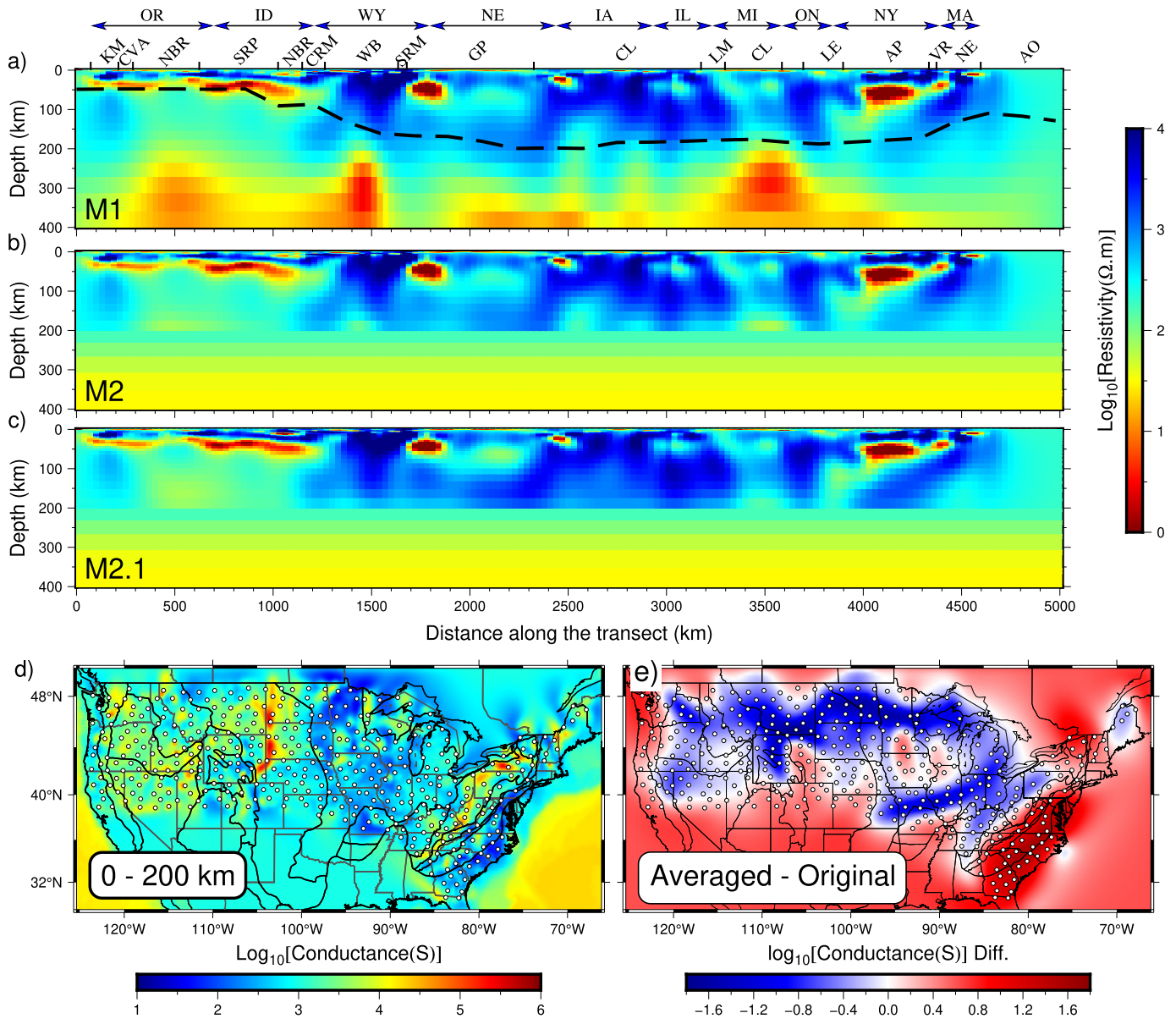

Fig. 3. East-west transect at latitude 42.5 (line AA' in Fig. 2c) from three models: (a) the initial model M1, (b) model M2 modified from (a) by replacing 3D resistivity values in each layer below 200 km by 1D layer averages, and (c) model M2.1 obtained by restarting inversion from (b) with 1D layers below 200 km frozen. The black dashed line in (a) indicates the LAB derived from seismic model (Priestley et al., 2018). (d) The 0–200 km conductance of M1. (e) conductance difference between M1 and M2, integrated over 200–400 km. Note that the total conductance in this depth range for M2 is 3.642 in log10 domain; variations in M1 conductance exceed ±1 order of magnitude. OR: Oregon; ID: Idaho; WY: Wyoming; NE: Nebraska; IA: Iowa; IL: Illinois; MI: Michigan; ON: Ontario; NY: New York; MA: Massachusetts; KM: Klamath Mountains; CVA: Cascade Volcanic Arc; NBR: Northern Basin and Ran; CRM: Central Rocky Mountains; WB: Wyoming Basin; SRM: Southern Rocky Mountain; GP: Great Plains; CL: Central Lowlands; LM: Lake Michigan; LE: Lake Eire; AP: Appalachian Plateaus; VR: Valley and Ridge; NE: New England; AO: Atlantic Ocean.

notation M#, with the initial inverse model discussed above referred to as M1, and the final preferred model as M5. A brief description of all models, including intermediate models M2–M4 discussed in the course of this section, are provided in Table 1, along with some summary misfit statistics.

4.1. A 1D model

As a first step we modified model M1 for depths below 200 km by replacing 3D resistivity values with 1D layer averages (Fig. 3a to 3b), computed as the arithmetic mean of log resistivity over the area with data coverage. The averaged resistivity in each slice in this depth range is noted in Fig. 2(e-h). The conductivity on average increases with depth to the top of mantle transition zone (MTZ; ~410–660 km), and then decreases. Note that in M1 the MTZ is too resistive compared with previous studies using longer period data (e.g., Kuvshinov and Olsen, 2006; Kelbert et al., 2009). The nRMS of the resulting modified model (M2) increases, but only slightly, to 2.07. The large lateral variations seen in the deeper layers in Fig. 2 apparently have a relatively small effect on model responses. Areas with a shallow LAB and/or high conductivity layers in the lithosphere, such as the North Basin and Range, are fit nearly as well with model M2 as with M1 (Fig. 4a), as also seen in the phase tensor plots of Fig. S4. This may reflect limited penetration in this area, but in fact the conductance of M1 over the 200–400 km depth range in this area is similar to the continental average (Fig. 3e), so M2 does not differ much from M1 in this area. It is worth noting that if the prior model resistivity of 200 Ω.m is used instead of the layer averages, misfit increases significantly at almost all sites (Fig. S5) and global nRMS increases to 2.41. We

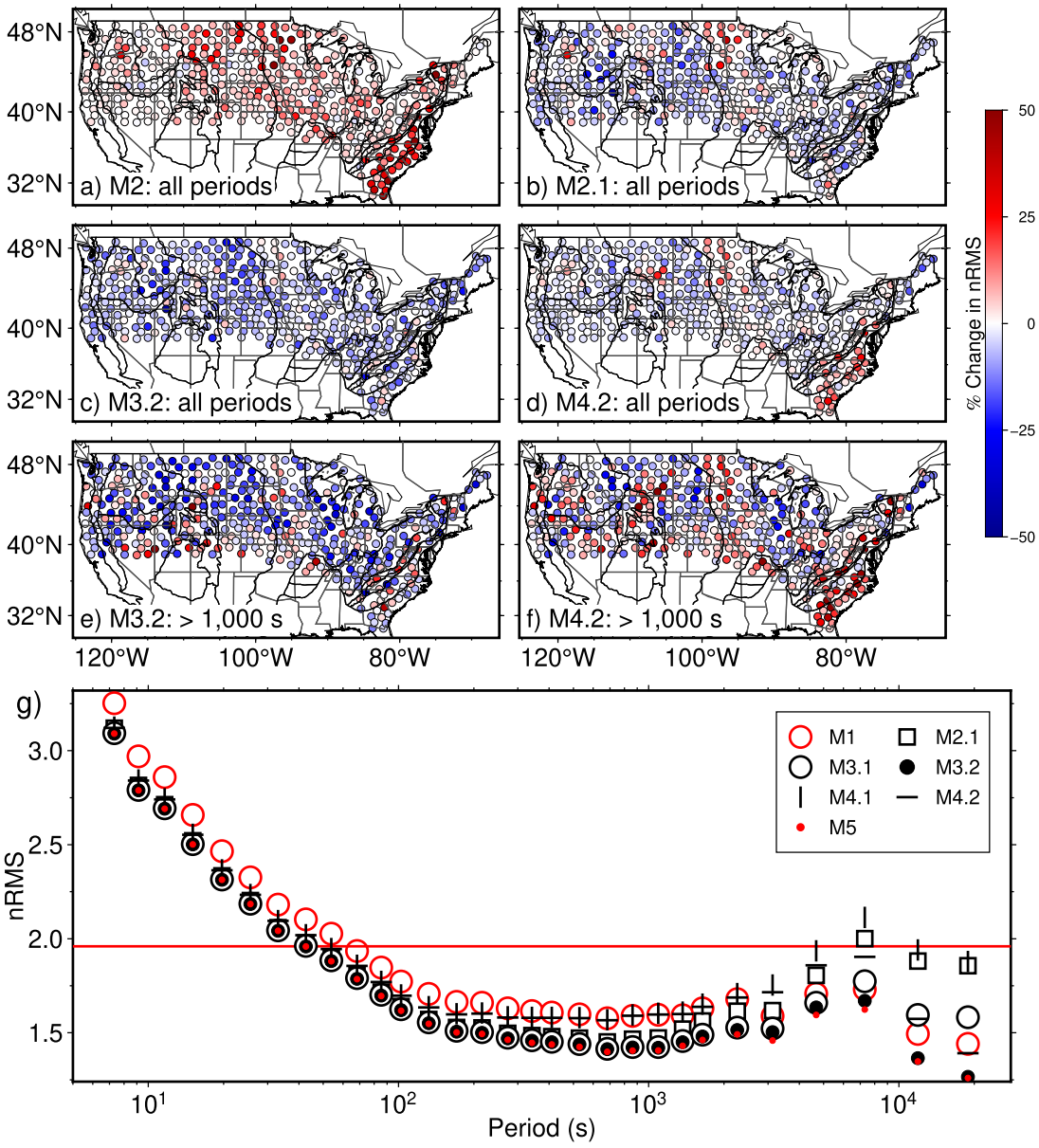

Fig. 4. Site-by-site change in nRMS of various models discussed in the text, relative to M1. Positive changes (red) indicate worse, and negative changes (blue) better fits. Panels (a-d) show results for all periods, (e-f) for periods exceeding 1,000 s. Panel (g) shows nRMS as a function of period and the fit for all the models is with respect to the measured data. Note that the nRMS for M6 is almost the same as that for M5 so that only M5 is shown. The horizontal red line shows the total nRMS (1.96) of the initial model M1.

conclude that there is some constraint on resistivity below 200 km, even beneath areas with shallow conductive features.

We next restart the inversion with the deep layered structure frozen, and all inversion parameters kept as for M1. As shown in Fig. 4b, fits for this model (M2.1) are actually improved relative to those obtained with M1 for the majority of sites, and the global nRMS is reduced to 1.87. Certainly, the best fitting model without the constraints on 200–400 km should have a smaller misfit than the one with the constraints. The observed reduction in nRMS reflects the challenges of 3D inversion, and the fact that linearized searches can get stuck in local minima. In any event, this shows that one can achieve a good fit without significant deep structure, and calls into question how reliable the deep features are. Note that above 200 km, almost all features of model M2.1 are indistinguishable from the initial model M1, as illustrated in Fig. 3c.

However, looking at the nRMS as a function of period (Fig. 4g black squares), we see that the improvement in fit is only at periods shorter than 3,000 seconds; at longer periods the fit of model M2.1 is actually degraded relative to M1. A closer look at the long-period phase data, which is less affected by galvanic distortion, reveals two problems. First, for model M2.1 predicted phases at the longest periods are consistently lower than observed, as illustrated for the yx-mode (corresponding to E-W electric fields) in Fig. 5. This systematic discrepancy, which also is seen in the xy-mode (Fig. S6), indicates that resistivity in the Earth decreases more rapidly with depth than in the model M2.1 (e.g., Simpson and Bahr, 2005). Second, careful examination of the phase differences (Fig. 5), reveals that phases along the north margin are consistently low starting at 3,000 s. In contrast to the first problem, this does not occur for the xy-mode phase (see Fig. S6).

Compared with published laboratory data (e.g., Huang et al., 2005) and field-based induction studies (e.g., Kuvshinov and Olsen, 2006), resistivity of the MTZ is expected to be close to 10 Ω.m, while the resistivity in the MTZ for M2.1 (i.e., the layer average

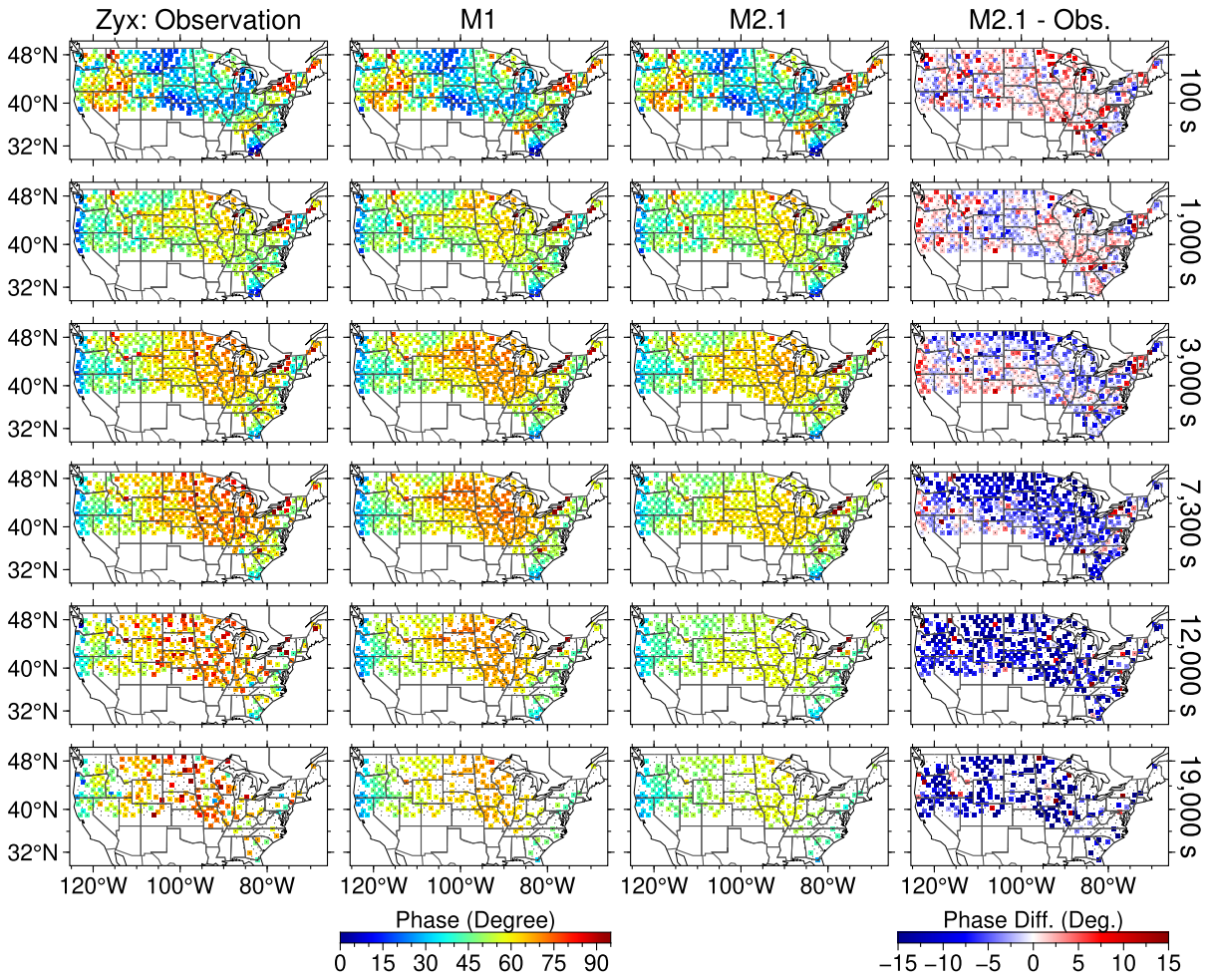

Fig. 5. Phase for yx-mode, for observations, and computed for M1 and M2.1. The last column shows the difference between observations and M2.1.

from M1) is about 50 Ω.m. The systematically low phases at long periods might plausibly be corrected by imposing a more realistic resistivity for the MTZ. With regard to the second issue, note that BC for all inversion runs discussed so far were derived from a simple (half-space except for the ocean) nesting model, which is more resistive than the deep layered structure frozen in the M2.1 inversion. The mismatch between BC and the assumed layered structure is a likely cause of the phase problem along the northern boundary. This does not occur in the xy-mode, for which BC (specified tangential fields) are zero along this boundary. Similar biases are not found for either mode along other boundaries, likely because the southern boundary is further from most of the data sites, and any effects at the eastern and western boundaries (which might now be expected in the xy-mode) are masked by complications associated with the coastline, and the high conductivities of the ocean.

For our subsequent inversion and forward model runs, we modified the coarse-grid nesting model, setting the deep layered structure as in M2, and used these forward solutions for BC. Using these BC, but otherwise following the inversion procedure outlined above, yields a model (M3.1) with significantly decreased boundary effects (Fig. S7). Data fit is also slightly improved (Fig. 4g black circles), with a nRMS of 1.83. Next we modified resistivity in the MTZ to 13 Ω.m, based on the model of Kuvshinov and Olsen (2006), and ran the inversion again, to get model (M3.2). With this modification model fit improves for all periods (Fig. 4g black dots), with the global nRMS reduced to 1.82. This clearly shows that the EarthScope TA data have some resolution to depths of the MTZ, which is required to be moderately conductive as previous global studies have found (Kuvshinov and Olsen, 2006). The improvement in fit can also be seen in the phase data (Fig. S8-S9). Furthermore, the main features shallower than 200 km remain unchanged from the initial model obtained without any constraints on deep structure (Fig. S10). The very subtle adjustments by the inversion would have no significant influence on the interpretation of imaged lithospheric structures.

Following the same strategy, we tested setting the cutoff depth for averaging deep structure to 150 km. As shown in Fig. 4g (vertical and horizontal black bars), noticeably poorer fits, especially beyond 3,000 seconds, are obtained for both variants: models M4.1 and M4.2, respectively without and with the conductive MTZ. This is also clear at the site-by-site change in nRMS of M4.2 especially for periods great than 1,000 s (Fig. 4f). We take this as clear evidence that lateral variations between 150 and 200 km depth are required by the data.

4.2. Variations in deep resistivity

The overall fit was improved with the deep 1D constraint below 200 km, but there are regions of poorer fit (Fig. 4e). These anomalous regions occur in regions of thick resistive lithosphere, especially the Superior Craton (Fig. 2(c-d)), indicating some deep variations (perhaps more deeply extending resistive material) are required here. Similarly, localized increases in misfit for the 150 km tests suggests that the resistive lithosphere beneath the SEUS extends to approximately 200 km, as concluded by Murphy and Egbert (2017). In fact, much of the reduction in misfit occurs at

short periods (< 1,000 s), while for the long periods (> 1,000 s) sensitive to deeper structure (Fig. 7), fits are actually worse in a few more regions, suggesting a more widespread need for at least modest lateral variations in resistivity below 200 km.

We explore these possible variations by looking more carefully at the site-by-site phase misfits considered above. All of the models discussed exhibit spatially coherent phase misfits. Here we focus on the model M3.2 for long periods. To more clearly emphasize the large scale patterns, and to eliminate some of the evident outliers of phase difference (Fig. S11), we applied a median smoother to the raw phase misfit plots. We tried two approaches: (a) for each data location find the 10 nearest sites, then take the median phase difference among the resulting set of 11 sites; (b) take the median over all sites within a radius of 300 km. Results are indistinguishable (Fig. S12), so for subsequent analysis we focus on the first approach. As illustrated in Fig. 6, the smoothed phase differences are just a few degrees (see also Fig. S13).

Patterns for xy- and yx-modes are not the same, but have some similarity. In general, especially at 3,000–7,300 s, modeled phases are too high in the south, and too low in the north for both modes. However there are also significant differences between modes, especially west of the Appalachians, at shorter periods in the SEUS, and along the west coast. Additionally, there is at least some similarity between the smoothed phase misfits (Fig. 6) and the conductance (200–400 km) difference between M1 and the layer averages used for M2-M4 (Fig. 3e), with regions where the layer averages are more resistive than M1 (blue in Fig. 3e; mostly in the north/central parts of the array) tending to have negative phase misfits (blue in Fig. 6). To increase phases in these areas, vertical gradients of conductivity should increase locally. Thus, these areas might well need to be more conductive than the average, as in M1.

As a simple test of sensitivity of long period phase to large scale deep resistivity variations, we did forward calculations with resistivity between 200–400 km uniformly shifted up and down by a quarter of an order of magnitude. For these calculations M3.2 was used as the base, with no changes in shallow (<200 km) resistivity. The resulting change in modeled phases are shown for the xy-mode in the first two columns of Fig. 7. To see the effects of large scale lateral variation in this depth range we also did a "checkerboard" test, with alternating patches of increased and decreased resistivity. Results of this test, and sensitivity to increasing conductivity of the MTZ are shown in the last two columns of Fig. 7. Sensitivities for the yx-mode are very similar (Fig. S14), especially for the MTZ. The phase shifts produced by variations in the upper mantle are roughly 2 degrees, with amplitudes decreasing for periods beyond 3,000 s. Sensitivity for changes in the MTZ of course peak at longer periods, near 12,000 s. Even with the uniform change in layer resistivity there is some spatial structure, and some difference between increasing versus decreasing resistivity. However the phase sensitivity is very smooth.

The spatially variable response can be understood in terms of conductance of shallower layers (Fig. 3d). For example, the high lithosphere conductivities in the North Basin and Range screens the response at 1,000 s period. At 7,300 s the sign of the response flips in the mid-continent area when resistivity is increased. Shallow conductance is lowest in this region, so at a fixed period we see more deeply, and the high conductivities of the MTZ are already being sensed. Increasing the 200–400 km resistivity increases the gradient at the top of the MTZ, and therefore increases phases. We also see the MTZ when resistivity is reduced. In this case we reduce gradients at the top of the MTZ, and thus relatively reduce phases. This shows up as the weaker phase increase at 7,300 s, and the subtle phase decrease at 12,000 s. At the longest periods we clearly see the MTZ everywhere, with the sign of the response for 200–400 km perturbations reversed. In summary, the response in phase shift is quasi-uniform across the array. Deviations from this simple picture can be explained by the variable penetration depth of the source fields at a fixed period, due to variations of conductance of the overlying layers. Checkerboard results are quite consistent with the uniform layer results, indicating the response is local at the large horizontal scales considered.

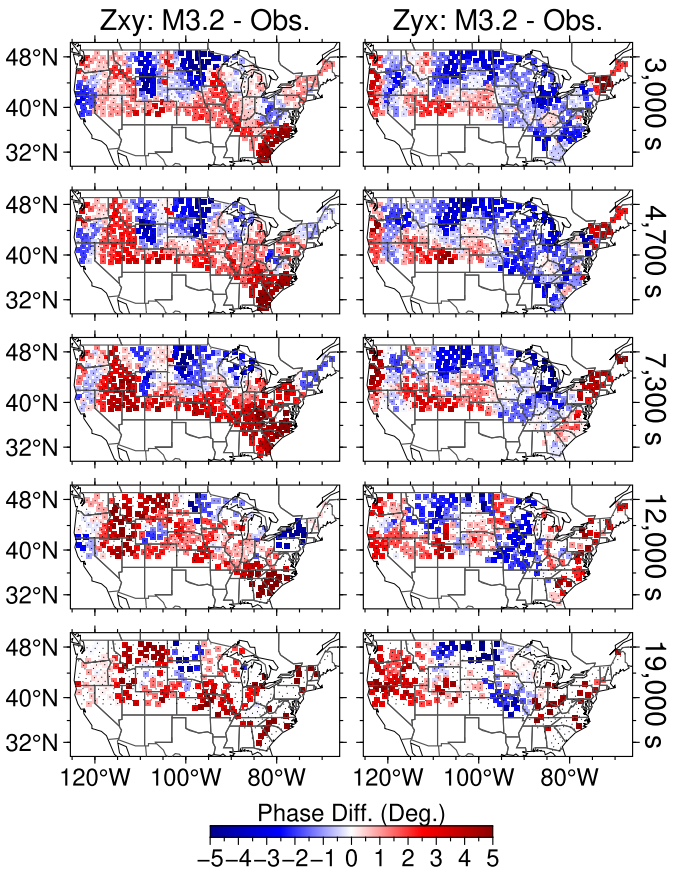

Fig. 6. Smoothed phase difference between observations and those derived from model M3.2 for the longest five periods at all sites. See Fig. S11 for unsmoothed differences.

In fact, the phase deviation of the long periods (> 3,000 s) for the above sensitivity tests are within ± 2.5°, which is about the same as the standard deviation of the smoothed residuals between measured data and predictions from M3.2 (Fig. S13). Therefore, roughly half an order of magnitude (total range) in resistivity should account for the majority of smoothed phase differences. In an effort to find such a model, we restart the inversion from M3.2, with the whole model domain frozen, except for depths of 200–400 km. For this inversion we modify the data and error bars. The modified data are generated by subtracting the smoothed phase differences (plotted for long periods in Fig. 6) from the computed phases for M3.2. The resulting phases ϕ are similar to, but spatially smoother than, the original phases, since small scale variations and some noise is eliminated by the smoothing. (Note that if we subtracted the unsmoothed phase differences from the M3.2 phases, we would recover the observations exactly.) A similar procedure is applied to $log(\rho_a)$, for both modes, and these modified ϕ, ρ_a (only for off-diagonal components of the impedance in geographic coordinates) are used as input data for the inversion. The phase data is less affected by galvanic distortion, so we focus on fitting phases. To do this we set error bars for phases to a small value (1.5°) and for apparent resistivities to a large value (100%).

For this inverse solution, which we refer to as M5 (Fig. 8(a-d)), data fits (with respect to the original measured data) are slightly improved with a global nRMS 1.81 (Fig. 4g red dots). This good data fit is also obvious in the phase tensor (Fig. S4). The ampli-

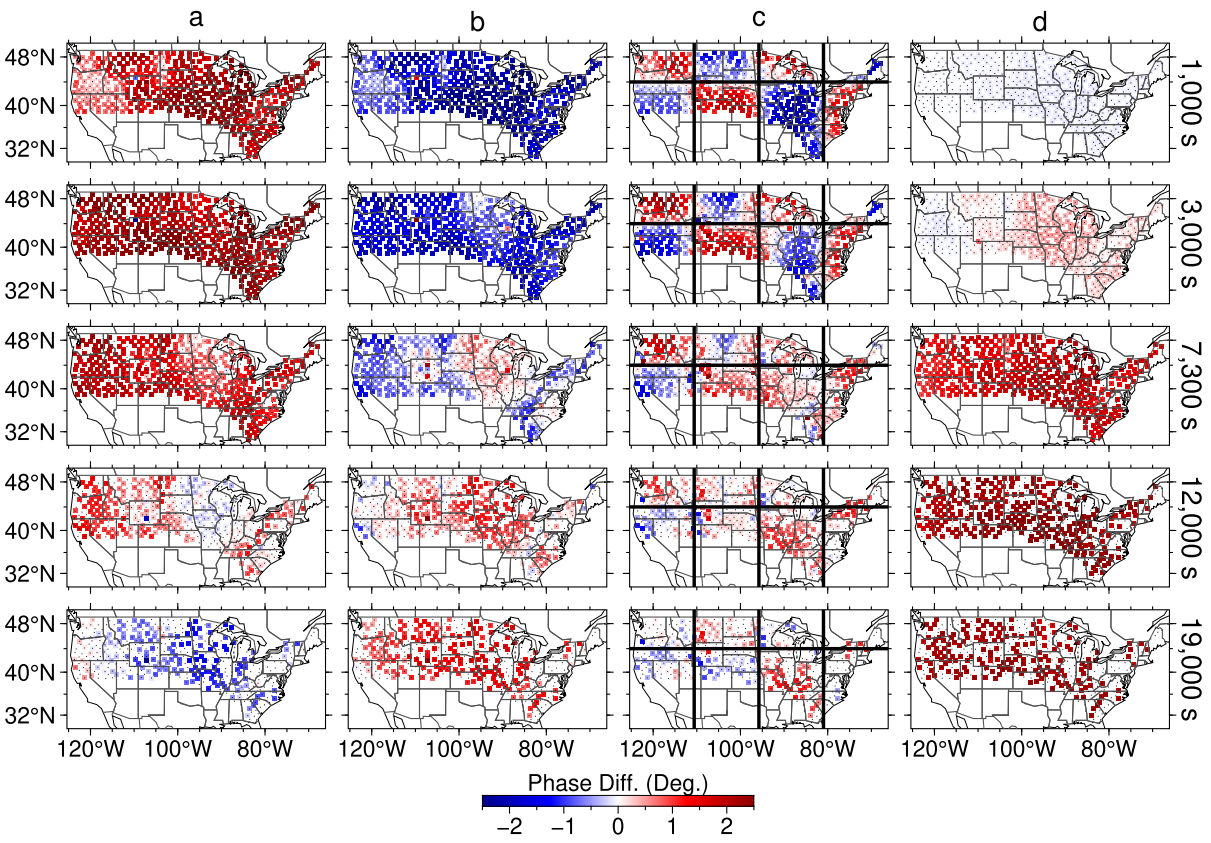

Fig. 7. Sensitivity of the xy-mode phase to uniform changes in deep resisitivity. Resistivity of model M3.2 was reduced over the 200-400 km depth range by a quarter of an order of magnitude (a), and increased by a similar amount (b). The column (c) shows sensitivity to changes with a checkerboard pattern of the same magnitude, again uniformly over depths of 200–400 km. The column (d) shows sensitivity to a 1/4 order reduction in resistivity of the MTZ.

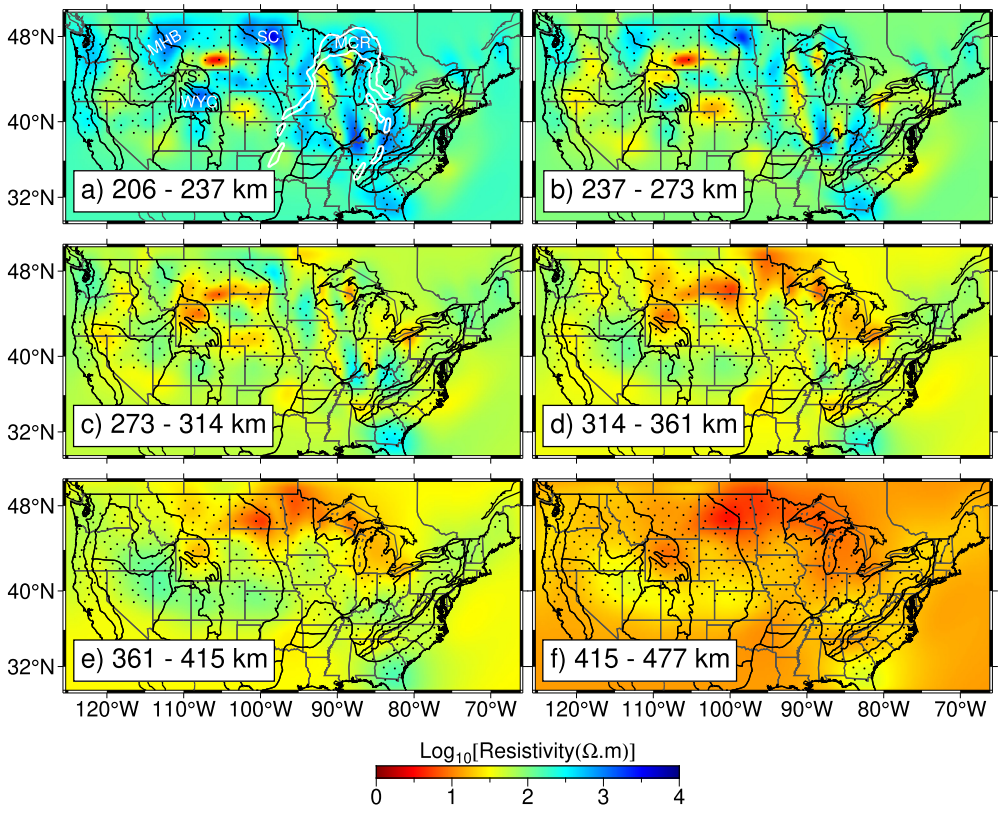

Fig. 8. Depth sections for resistivity model M5 (a-d) and M6 (e-f). (a-d) are comparable to Fig. 2(e-h). MHB: Medicine Hat Block; WYC: Wyoming Craton; SC: Superior Craton; YS: Yellowstone; MCR: Midcontinent Rift.

tude of smoothed phase differences are decreased at short periods (Fig. S15), but there is little to no improvement for longer periods. In contrast to model M3.2, there is little to no consistency between modes in the smoothed phase residuals for model M5. It is also worth noting that phase differences for the original residuals at the two longest periods are often quite large, consistent with the error bars at these periods (Fig. S2). Certainly some of scatter (and some of the smoothed phase difference) result from noise in the response estimates.

5. Geophysical interpretation

As the major mineral of the upper mantle, the electrical conductivity of olivine has been widely studied (e.g., Constable, 2006; Dai and Karato, 2014) and used to interpret resistivity models derived from MT (e.g., Meqbel et al., 2014; Yang et al., 2015; Murphy and Egbert, 2017). At mantle temperatures, the electrical conduction of silicate minerals under dry condition is enabled by small polaron diffusion (electron holes hopping between ferrous Fe^{+2} and ferric Fe^{+3} ion), and at higher temperature about 1300°C is dominated by ionic diffusion (Constable, 2006; Jones et al., 2009). Constable (2006) proposed a standard electrical olivine (SEO3) model incorporating both of these conduction mechanisms. Note that the quartz–fayalite–magnetite redox buffer were chosen for SEO3 that we use here. The model of Yoshino et al. (2009) and Gardés et al. (2014) for dry olivine also includes both of these conduction mechanisms. As shown in Fig. 9, for dry olivine similar resistivities are obtained from all of these studies.

Electrical conductivity of silicate minerals is highly sensitive to water content, or more precisely, hydrogen as defects in nominally anhydrous mantle minerals, so conductivity can place constraints on the hydration of the upper mantle (Karato, 2011). Unfortunately, there remain significant discrepancies between results from different laboratories on water assisted conductivity of olivine (e.g., Dai and Karato, 2014; Yoshino et al., 2009) and wadsleyite (e.g., Yoshino and Katsura, 2012; Dai and Karato, 2009), limiting the precision of inferences that can be made from resistivity estimates obtained from geophysical data. By considering all experimental measurements on conductivity of hydrous olivine, Gardés et al. (2014) proposed a unified hydrous olivine electrical conductivity law. In Fig. 9 we show conductivity estimates for the upper mantle derived from the Gardés et al. (2014) model, as well as the SEO3 model, and from selected primary references. The temperature-depth relation used here is from Karato (2011). Note that all but Gardés et al. (2014) used Paterson calibration (Paterson, 1982), which has been found to underestimate the water in olivine by a factor of 3–3.5 (Bell et al., 2003). We have normalized all results to the alternative Bell calibration, by multiplying water content for olivine in the reported laboratory results by a factor of 3. Paterson calibration appears to be accurate for wadsleyite (Hirschmann et al., 2005), so we make no adjustments for this MTZ mineral here.

As shown in Fig. 9, the average profile is reasonably consistent with a nearly dry mantle, up to depths of ∼275 km. SEO3 would require very modest hydration, ignoring the possible uncertainty from temperature and oxygen fugacity. At greater depths (down to 400 km) the average profile requires some degree of hydration. The model of Gardés et al. (2014) would imply ∼150 ppm, which is in good agreement with the average water content of the upper mantle (50–200 ppm) inferred from mid-ocean ridge basalt (MORB) as summarized by Hirschmann (2006). In contrast, it appears unreasonable amounts of water would be required to explain even the average profile using the model of Yoshino et al. (2009), even exceeding the ∼840 ppm that would induce melting at depths of 300–400 km with a mantle temperature profile similar to ours (Hirschmann et al., 2009; Tenner et al., 2012). We consider pervasive melt 300–400 km beneath the US highly unlikely.

There are lateral variations in deep resistivity (200–400 km) in both M1 and M5, but the variations in M5 are subtle by comparison (Fig. 8). However, there are some similarities between the two models in terms of gross spatial patterns, with higher conductivities in the upper mantle across the north-central part of the continental US in both cases (compare Fig. 2(e-h), Fig. 8). There are also significant differences between the two models. For example, the prominent deep resistive feature ($> 1,000\,\Omega$.m) in M1 extending to 400 km depth beneath the SEUS is absent in M5, and is clearly not required by the data, as discussed already in Murphy and Egbert (2017, 2019). Indeed, laboratory results for conductivity of dry olivine (Constable, 2006) would require unacceptably low temperatures (∼1200°C) over the depth range 200–400 km, for the resistivities of $> 1000\,\Omega$.m that are seen in M1.

Between 200-400 km depth, even the highest conductivities in M5 are only a quarter of an order of magnitude above the average, which if interpreted solely in terms of water, would imply 300 ppm by the model of Gardés et al. (2014) (Fig. 9). However, to interpret the high conductivity (∼1–3 Ω.m) east of the Rocky Mountains in M1 (200–275 km), the laboratory result most sensitive to water (Dai and Karato, 2014) would imply extremely high water content, at least ∼2, 000 ppm. This exceeds the ∼1355 ppm, required to initiate melting at 250 km depth (Ardia et al., 2012). As shown in Fig. 9, to explain the extremely high conductivity ∼2 Ω.m of M1 of 200–275 km, at least 2% melt would be required (Laumonier et al., 2017). We consider such high melt fractions to be highly unlikely at these depths, especially since there is no seismic evidence to support this interpretation. At such depths interconnected graphite films or sulfide minerals, often cited to explain high conductivities in the lithosphere, would not be stable and thus can be ruled out (Selway, 2014). We conclude the subtle variations in upper mantle (asthenospheric) resistivity of M5 are much more physically reasonable than the rather extreme variations exhibited by M1.

Fig. 8 shows some interesting variations in deep resistivity. At shallower depths (a-b), higher resistivities are consistent with deep cratonic roots for the Medicine Hat Block, Wyoming Craton, and Superior Craton, extending to ∼250 km. In addition, the two arms of the Midcontinent Rift inferred from potential field and surface geology (Stein et al., 2018) correlate with high resistivity streaks which wrap around through northern Michigan, and may represent deep roots of the Midcontinent Rift. If the mantle in all of these resistive areas is dry, which is plausible given the geologic history, temperatures of ∼1200–1260°C could explain the modeled resistivities, based on SEO3. At depths larger than ∼250 km, the Yellowstone hot spot shows up as a conductive feature. Less than 300 ppm of water (Gardés et al., 2014) would explain this feature; melt is not necessary (Karato, 2011) and is unlikely, given the inferred water content. As shown in Fig. 9, excess temperatures of ∼120°C could also account for this feature (Constable, 2006), which is comparable with estimates of a plume thermal anomaly of ∼100°C obtained from seismic tomography (Smith et al., 2009). As seismological observations are very sensitive to temperature but only weakly sensitive to water content (Karato, 2011), a thermal interpretation is most reasonable here, although the seismic and MT anomalies are not exactly spatially coincident. At great depth (∼300 km) the highest conductivities are beneath the North-central part of the array, in good agreement with the phase as shown in Fig. 6. This suggests that beneath the older parts of the continent water content is elevated in the asthenospheric upper mantle, relative to other areas. Again, modest variations in temperature could also explain the resistivity patterns.

We did not thoroughly test the resistivity and possible variations of MTZ because of the relatively large data error at the long periods (Fig. S2) that are most sensitive to resistivity at this depth (Fig. 7 and S5). We found a moderately conductive MTZ (13 Ω.m)

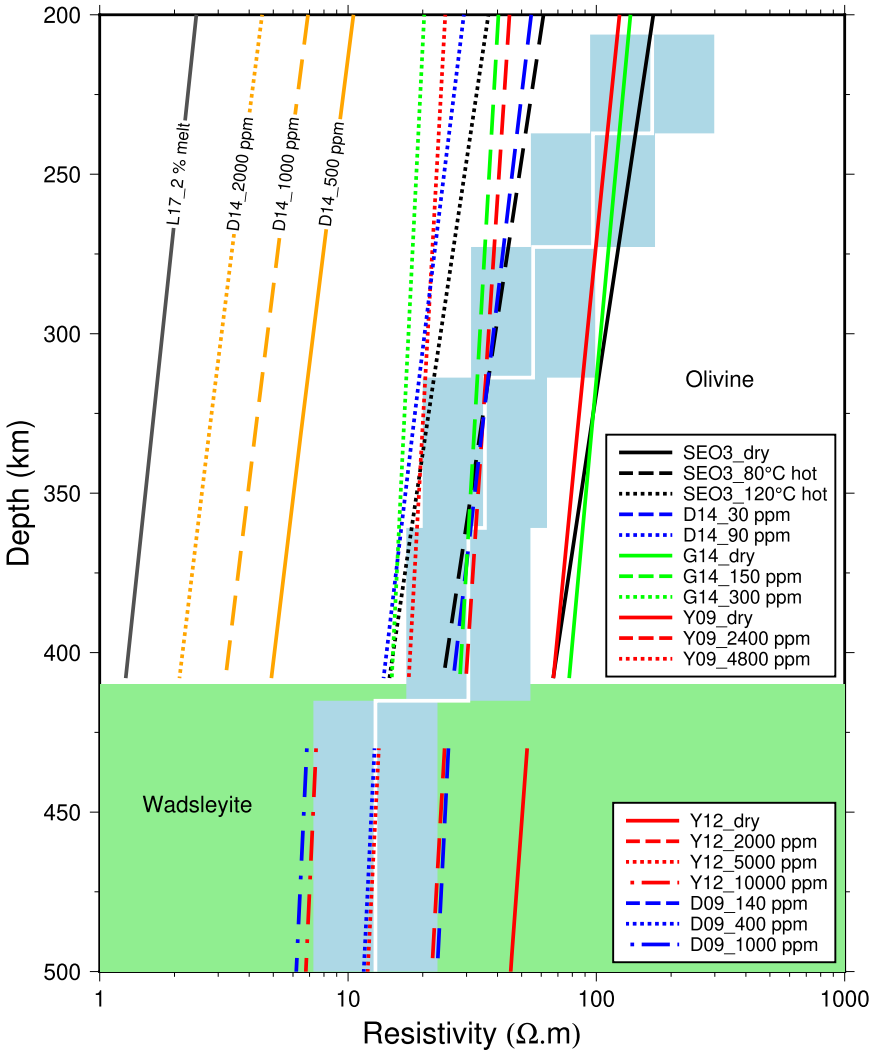

Fig. 9. Comparison of the 1D layered average electrical resistivity model with selected models based on laboratory results, for dry and hydrated olivine. Light blue regions surrounding the resistivity-depth profile (white line) represent variations within $\pm 1/4$ order of magnitude. SEO3: Constable (2006); D14: Dai and Karato (2014); G14: Gardés et al. (2014); Y09: Yoshino et al. (2009); Y12: Yoshino and Katsura (2012); D09: Dai and Karato (2009); L17: Laumonier et al. (2017).

significantly improved fit to the long period data, but other resistivity profiles for the MTZ, (e.g., depth-dependent as would be suggested by Huang et al. (2005)) were not tested. As shown in Fig. 9, to explain this resistivity water content of 400 ppm would be required by the model of Dai and Karato (2009), while much more (5,000 ppm) would be required assuming the model of Yoshino and Katsura (2012). Either water content is at least possible, given the high solubility of water (at least $\sim$10,000 ppm) in the dominant MTZ mineral Wadsleyite (Karato, 2011). The approach used to obtain M5 was extended to explore possible variations in resistivity of the MTZ, by unfreezing the model below 400 km. The resulting model (M6) is essentially unchanged for depths of 200–400 km. Deeper variations in this model are shown in Fig. 8 (e-f). These show a strong correlation with shallower variations, but this may mostly reflect poor vertical resolution of the MT data. Exploration of variations in MTZ conductivity would almost certainly require longer period data than are available from the EarthScope TA.

6. Discussion and conclusions

We inverted long-period MT TA data spanning the North American continent, and then tested the robustness of deep ($>$ 200 km) features. Our results have implications both for MT inversion practice, and for the resistivity structure of the upper mantle beneath North America.

6.1. Inversion practice

When maximum penetration depths are a significant fraction ($\sim$1/3) of array aperture, 3D MT inversions typically result in relatively smooth deep structure (e.g., Kelbert et al., 2012). This reflects the diffusive nature of EM induction, with lateral resolution that scales with skin depth. As the area of data coverage increases, significant lateral variations in deep resistivity, even in the sub-lithospheric mantle, emerge (e.g., Meqbel et al., 2014; Yang et al., 2015). In our initial unconstrained inversion at continental-scale (i.e., M1) amplitudes of deep lateral variations are quite large, with both high and low resistivities that are physically unreasonable. However, much simpler models, with more sensible deep resistivities, fit the data at least as well. The fact that global misfits (for example, for M2.1) decrease when conductivity below 200 km is constrained to a layered structure demonstrates that M1 corresponds to a local minimum of data misfit. The ModEM non-linear conjugate gradients (NLCG) search strategy (Kelbert et al., 2014), which reduces the regularization factor when reductions in data misfit stall, perhaps results in local near-minima of data misfit, with only weak regularization. It is well known that for the 1D

MT inverse problem the global minimizer of data misfit occurs for the very singular D+ model (Parker, 1980). Minimizing data misfit with a linearized search scheme for 1D inversions results in similar "spikey" models (e.g. Smith and Booker, 1988; Egbert and Booker, 1992). The situation here perhaps bears some similarity.

Local minima are probably unavoidable with linearized inversion. However, within the framework of the ModEM scheme, we suggest that there might be some value in modifying the regularization parameter "cooling" strategy, which allows potentially large increases in model norm for very small reductions in misfit. In general, when using linearized inversion great care should be taken in testing important (and especially difficult to explain) structures. Indeed, modifying model parameters manually, and then restarting the inversion can sometimes jump out of a local minimum, and allow at least a somewhat more complete search of model space.

Our results provide an example of the pitfalls of blindly using a global measure, such as nRMS, to define model fit. More careful examination of residuals, grouped by periods, modes, and spatial location, can provide insight into what parts of the dataset are fit more poorly, and suggest strategies for improved imaging. Even with all of our efforts in this direction, we still see coherent patterns in residuals. These might reflect limitations in the inversion code. However, the patterns are not consistent between modes, and thus probably cannot be fit by any smooth isotropic model. Possibly these reflect small scale structures, which would be most reasonably modeled as anisotropic. It is also at least possible that subtle source effects in the very long period data contribute to the remaining misfit.

Our analysis demonstrates that MT data extending to 10,000-20,000 s can put constraints on resistivity down even to the transition zone. This conclusion is supported by "squeeze tests" (Fig. S5) which suggest sensitivity to 550 km, and all of the forward and inverse modeling results presented above (i.e., Figs. 4, 5, 7). Finally, our results demonstrate the need for care in treatment of BC. Specifying inaccurate tangential field components will make it impossible to fit data that are too near the boundary. This effect appears to be most severe in the mode corresponding to electric fields parallel to the boundary.

6.2. North American upper mantle

Although a model (such as M3.2) that is laterally uniform below 200 km depth fits the data nearly as well in terms of nRMS, there are systematic spatial patterns in residuals at long periods that are consistent with modest, and physically sensible, variations in deep resistivity. Our final results (M5) exhibits variations at depths of 200–400 km that bear some similarity to our initial model (M1), but are much smaller, within a quarter order of magnitude of the layer means. Plausible variations in water contents and/or temperature can explain these lateral variations in deep resistivity, with no requirement for melting.

Just below 200 km, the MT data are consistent with deep modestly resistive roots beneath cratons, extending to depths of ~250 km. One interesting resistive feature at these depths occurs in the mid-continent region. The geometry of this feature is remarkably similar to the two arms of the Midcontinent Rift (Stein et al., 2018) inferred from potential fields and surface geology. This may represent deep roots of the aborted rift system, possible representing dehydrated material that became stiff enough around 1.1 Ga to resist subsequent modifications. This feature deserves more careful testing in future work. In contrast, deep (> 200 km) roots are not required beneath the SEUS, as shown previously in Murphy and Egbert (2019).

At greater depths (~300 km) there is a clear tendency for lower resistivities in the north-central part of the array, mostly beneath areas of more resistive and thicker lithosphere. These can be explained by modest levels of hydration (< 300 ppm). Higher resistivities, and reduced hydration (< 150 ppm) prevail in most other areas. Interestingly there is a deep patch of reduced resistivity, near (but southeast of) the Yellowstone hotspot, extending into the MTZ. Again, this feature deserves more careful testing.

The EarthScope MT TA data does have some resolutions of MTZ conductivity, which we infer to be of order ~10–20 Ω.m on average, beneath North America. The spatial variations coherent with shallower depth (~300–400 km) may result from the vertical smoothing of the inversion, given the poor vertical resolution of the MT TA data at such great depths.

CRediT authorship contribution statement

Bo Yang: Conceptualization, Formal analysis, Investigation, Visualization, Writing – original draft. **Gary D. Egbert:** Conceptualization, Investigation, Methodology, Validation, Writing – review & editing. **Huiqian Zhang:** Formal analysis. **Naser Meqbel:** Methodology, Software. **Xiangyun Hu:** Funding acquisition, Supervision.

Declaration of competing interest

The authors declare that they have no known competing financial interests or personal relationships that could have appeared to influence the work reported in this paper.

Acknowledgements

We thank Lidong Dai for discussions of experimental studies on electrical conductivity in hydrated olivine. We thank Carol Stein for sharing the digital boundary map of Midcontinent Rift. We thank Bo Yang for sharing the electrical resistivity model of the Midcontinent Rift. We also thank two anonymous reviews for their comments and suggestions which helped to improve clarity of this manuscript. We would like to acknowledge high-performance computing support from Cheyenne (https://doi.org/10.5065/D6RX99HX) provided by NCAR's Computational and Information Systems Laboratory, sponsored by the National Science Foundation for ModEM inversions. The data used here are archived with Incorporated Research Institutions for Seismology (IRIS) and are freely available at http://ds.iris.edu/spud/emtf (Kelbert et al., 2011). All figures here were plotted by the Generic Mapping Tools (Wessel et al., 2013). This work was supported by the China Scholarship Council (grant No. 201906410023), the National Natural Science Foundation of China (grant No. 41630317), and the National Key Research and Development Program of China (grant No. 2018YFC1503705). Support for GE was provided by NSF grant EAR-1820688.

Appendix A. Supplementary material

Supplementary material related to this article can be found online at https://doi.org/10.1016/j.epsl.2021.117244.

References

Ardia, P., Hirschmann, M., Withers, A., Tenner, T., 2012. H2o storage capacity of olivine at 5–8 GPA and consequences for dehydration partial melting of the upper mantle. Earth Planet. Sci. Lett. 345, 104–116.

Avdeeva, A., Moorkamp, M., Avdeev, D., Jegen, M., Miensopust, M., 2015. Three-dimensional inversion of magnetotelluric impedance tensor data and full distortion matrix. Geophys. J. Int. 202 (1), 464–481.

Bedrosian, P.A., Feucht, D.W., 2014. Structure and tectonics of the northwestern United States from earthscope usarray magnetotelluric data. Earth Planet. Sci. Lett. 402, 275–289.

Bell, D.R., Rossman, G.R., Maldener, J., Endisch, D., Rauch, F., 2003. Hydroxide in olivine: a quantitative determination of the absolute amount and calibration of the IR spectrum. J. Geophys. Res., Solid Earth 108 (B2).

Caldwell, T.G., Bibby, H.M., Brown, C., 2004. The magnetotelluric phase tensor. Geophys. J. Int. 158 (2), 457–469.
Chave, A.D., Jones, A.G., 2012. The Magnetotelluric Method: Theory and Practice. Cambridge University Press.
Constable, S., 2006. Seo3: a new model of olivine electrical conductivity. Geophys. J. Int. 166 (1), 435–437.
Dai, L., Karato, S., 2009. Electrical conductivity of wadsleyite under high pressures and temperatures. Earth Planet. Sci. Lett. 287, 277–283.
Dai, L., Karato, S.-i., 2014. High and highly anisotropic electrical conductivity of the asthenosphere due to hydrogen diffusion in olivine. Earth Planet. Sci. Lett. 408, 79–86.
Egbert, G.D., 1989. Multivariate analysis of geomagnetic array data: 2. Random source models. J. Geophys. Res., Solid Earth 94 (B10), 14249–14265.
Egbert, G.D., Booker, J.R., 1986. Robust estimation of geomagnetic transfer functions. Geophys. J. Int. 87 (1), 173–194.
Egbert, G.D., Booker, J.R., 1992. Very long period magnetotellurics at Tucson observatory: implications for mantle conductivity. J. Geophys. Res., Solid Earth 97 (B11), 15099–15112.
Egbert, G.D., Kelbert, A., 2012. Computational recipes for electromagnetic inverse problems. Geophys. J. Int. 189 (1), 251–267.
Gardés, E., Gaillard, F., Tarits, P., 2014. Toward a unified hydrous olivine electrical conductivity law. Geochem. Geophys. Geosyst. 15 (12), 4984–5000.
Goes, S., van der Lee, S., 2002. Thermal structure of the North American uppermost mantle inferred from seismic tomography. J. Geophys. Res., Solid Earth 107 (B3), ETG-2.
Grayver, A.V., van Driel, M., Kuvshinov, A.V., 2019. Three-dimensional magnetotelluric modelling in spherical Earth. Geophys. J. Int. 217 (1), 532–557.
Hirschmann, M.M., 2006. Water, melting, and the deep Earth H_2O cycle. Annu. Rev. Earth Planet. Sci. 34, 629–653.
Hirschmann, M.M., Aubaud, C., Withers, A.C., 2005. Storage capacity of H_2O in nominally anhydrous minerals in the upper mantle. Earth Planet. Sci. Lett. 236 (1–2), 167–181.
Hirschmann, M.M., Tenner, T., Aubaud, C., Withers, A., 2009. Dehydration melting of nominally anhydrous mantle: the primacy of partitioning. Phys. Earth Planet. Inter. 176 (1–2), 54–68.
Huang, X., Xu, Y., Karato, S.-i., 2005. Water content in the transition zone from electrical conductivity of wadsleyite and ringwoodite. Nature 434 (7034), 746–749.
Imamura, N., Schultz, A., 2020. Quality estimation of magnetotelluric impedance tensors using neural networks. Lead. Edge 39 (10), 702–710.
Jones, A.G., Evans, R.L., Eaton, D.W., 2009. Velocity–conductivity relationships for mantle mineral assemblages in archean cratonic lithosphere based on a review of laboratory data and Hashin–Shtrikman extremal bounds. Lithos 109 (1–2), 131–143.
Karato, S.-i., 2011. Water distribution across the mantle transition zone and its implications for global material circulation. Earth Planet. Sci. Lett. 301 (3–4), 413–423.
Kelbert, A., Schultz, A., Egbert, G., 2009. Global electromagnetic induction constraints on transition-zone water content variations. Nature 460 (7258), 1003–1006.
Kelbert, A., Egbert, G., Schultz, A., 2011. Iris dmc data services products: Emtf, the magnetotelluric transfer functions. National Geoelectromagnetic Facility Technical Report.
Kelbert, A., Egbert, G.D., deGroot Hedlin, C., 2012. Crust and upper mantle electrical conductivity beneath the Yellowstone hotspot track. Geology 40 (5), 447–450.
Kelbert, A., Meqbel, N., Egbert, G.D., Tandon, K., 2014. Modem: a modular system for inversion of electromagnetic geophysical data. Comput. Geosci. 66, 40–53.
Kelbert, A., Bedrosian, P.A., Murphy, B.S., 2019. The first 3d conductivity model of the contiguous United States: reflections on geologic structure and application to induction hazards. In: Geomagnetically Induced Currents from the Sun to the Power Grid, pp. 127–151.
Kuvshinov, A., Olsen, N., 2006. A global model of mantle conductivity derived from 5 years of CHAMP, Ørsted, and SAC-C magnetic data. Geophys. Res. Lett. 33 (18).
Laumonier, M., Farla, R., Frost, D.J., Katsura, T., Marquardt, K., Bouvier, A.-S., Baumgartner, L.P., 2017. Experimental determination of melt interconnectivity and electrical conductivity in the upper mantle. Earth Planet. Sci. Lett. 463, 286–297.
Meqbel, N.M., Egbert, G.D., Wannamaker, P.E., Kelbert, A., Schultz, A., 2014. Deep electrical resistivity structure of the northwestern US derived from 3-D inversion of USArray magnetotelluric data. Earth Planet. Sci. Lett. 402, 290–304.
Miensopust, M.P., 2017. Application of 3-d electromagnetic inversion in practice: challenges, pitfalls and solution approaches. Surv. Geophys. 38 (5), 869–933.
Murphy, B.S., Egbert, G.D., 2017. Electrical conductivity structure of southeastern North America: implications for lithospheric architecture and Appalachian topographic rejuvenation. Earth Planet. Sci. Lett. 462, 66–75.
Murphy, B.S., Egbert, G.D., 2019. Synthesizing seemingly contradictory seismic and magnetotelluric observations in the southeastern United States to image physical properties of the lithosphere. Geochem. Geophys. Geosyst. 20 (6), 2606–2625.
Parker, R.L., 1980. The inverse problem of electromagnetic induction: existence and construction of solutions based on incomplete data. J. Geophys. Res., Solid Earth 85 (B8), 4421–4428.
Paterson, M., 1982. The determination of hydroxyl by infrared absorption in quartz, silicate glasses and similar materials. Bull. Minéral. 105 (1), 20–29.
Patro, P.K., Egbert, G.D., 2008. Regional conductivity structure of Cascadia: preliminary results from 3d inversion of usarray transportable array magnetotelluric data. Geophys. Res. Lett. 35 (20).
Priestley, K., McKenzie, D., Ho, T., 2018. A lithosphere–asthenosphere boundary—a global model derived from multimode surface-wave tomography and petrology. In: Lithospheric Discontinuities, pp. 111–123.
Schultz, A., Egbert, G., Kelbert, A., Peery, T., Clote, V., Fry, B., Erofeeva, S., 2018. Staff of the national geoelectromagnetic facility and their contractors (2006–2018), usarray TA magnetotelluric transfer functions. https://doi.org/10.17611/DP/EMTF/USARRAY/TA. Technical report, DP/EMTF/USARRAY/TA. 2018.
Selway, K., 2014. On the causes of electrical conductivity anomalies in tectonically stable lithosphere. Surv. Geophys. 35 (1), 219–257.
Simpson, F., Bahr, K., 2005. Practical Magnetotellurics. Cambridge University Press.
Smith, J.T., Booker, J.R., 1988. Magnetotelluric inversion for minimum structure. Geophysics 53 (12), 1565–1576.
Smith, R.B., Jordan, M., Steinberger, B., Puskas, C.M., Farrell, J., Waite, G.P., Husen, S., Chang, W.-L., O'Connell, R., 2009. Geodynamics of the Yellowstone hotspot and mantle plume: seismic and GPS imaging, kinematics, and mantle flow. J. Volcanol. Geotherm. Res. 188 (1–3), 26–56.
Stein, C.A., Stein, S., Elling, R., Keller, G.R., Kley, J., 2018. Is the "Grenville Front" in the central United States really the Midcontinent Rift. GSA Today 28 (5), 4–10.
Tenner, T.J., Hirschmann, M.M., Withers, A.C., Ardia, P., 2012. H 2 o storage capacity of olivine and low-ca pyroxene from 10 to 13 GPA: consequences for dehydration melting above the transition zone. Contrib. Mineral. Petrol. 163 (2), 297–316.
Wannamaker, P.E., 2005. Anisotropy versus heterogeneity in continental solid Earth electromagnetic studies: fundamental response characteristics and implications for physicochemical state. Surv. Geophys. 26 (6), 733–765.
Wessel, P., Smith, W.H., Scharroo, R., Luis, J., Wobbe, F., 2013. Generic mapping tools: improved version released. Eos 94 (45), 409–410.
Yang, B., Egbert, G.D., Kelbert, A., Meqbel, N.M., 2015. Three-dimensional electrical resistivity of the North-central USA from earthscope long period magnetotelluric data. Earth Planet. Sci. Lett. 422, 87–93.
Yoshino, T., Katsura, T., 2012. Re-evaluation of electrical conductivity of anhydrous and hydrous wadsleyite. Earth Planet. Sci. Lett. 337, 56–67.
Yoshino, T., Matsuzaki, T., Shatskiy, A., Katsura, T., 2009. The effect of water on the electrical conductivity of olivine aggregates and its implications for the electrical structure of the upper mantle. Earth Planet. Sci. Lett. 288 (1–2), 291–300.